Eur. Phys. J. Appl. Phys. **54**, 33503 (2011)
DOI: 10.1051/epjap/2010100354

THE EUROPEAN PHYSICAL JOURNAL APPLIED PHYSICS

Regular Article

Modern electron microscopy resolved in space, energy and time

F. Carbone[a]

Laboratory of Ultrafast Spectroscopy, ISIC, École polytechnique fédérale de Lausanne, 1015 Lausanne, Switzerland

Received: 15 September 2010 / Accepted: 30 November 2010
Published online: 7 June 2011 – © EDP Sciences

Abstract. Recent pioneering experiments combining ultrafast lasers with electron-based technology demonstrated the possibility to obtain real-time information about chemical bonds and their dynamics during reactions and phase transformation. These techniques have been successfully applied to several states of matter including gases, liquids, solids and biological samples showing a unique versatility thanks to the high sensitivity of electrons to tiny amounts of material and their low radiation damage. A very powerful tool, the time-resolved Transmission Electron Microscope (TEM), is capable of delivering information on the structure of ordered and disordered matter through diffraction and imaging, with a spatial resolution down to the atomic limit (10^{-10} m); the same apparatus can distinguish dynamical phenomena happening on the time-scales between fs and ms, with a dynamic range of 12 orders of magnitude. At the same time, spectroscopic information can be obtained from the loss of kinetic energy of electrons interacting with specimens in the range of interband transitions and plasmons in solids, or charge transfers in molecules, all the way up to the atomic core levels with the same time-resolution. In this contribution, we focus on the recent advances in fs Electron Energy Loss Spectroscopy (FEELS), discussing the main results and their implications for future studies.

1 Introduction

1.1 The TEM

Soon after the discovery of the dual wave-particle nature of electrons, scientists realized its potential for obtaining images with higher resolution than that allowed by diffraction-limited optical microscopes. In the Thirties, the first electron based optics became available [1], and by 1933 the electron-based microscope broke the resolution limits of conventional optical microscopes in imaging a cotton fiber [1]. Further developments after world-war II allowed imaging of single atoms [2], and the concept of modern TEM was established [2]. In a TEM, atomic resolution can be reached in imaging even from a single atom thick sample, as recently demonstrated on graphene samples [3], or through proper reconstruction of a diffraction pattern [4]. Moreover, information about the composition of samples and their electronic configuration can be retrieved by analyzing the energy distribution of the electrons passing through the specimen [5,6]. The losses of kinetic energy that electrons undergo during inelastic scattering in materials, in fact, contain fingerprints of the elements included in the sample and their electronic configuration [7]. The TEM has been successfully applied to the study of biological specimens, molecular aggregates, and materials [8]. Still images and spectra of samples can be obtained in seconds or minutes of exposure, and movies of the evolution of a specimen could be obtained with a temporal resolution limited by the convolution of the response time for detection with that of the acquisition procedure; so far, seconds to ms time-resolution were obtained [9].

1.2 The time-resolved TEM

In order to push this limit into the time scale of atomic motions, the technology of electron imaging had to be combined with that of ultrafast lasers. In particular, in the modern pulsed TEM [9,10], fs lasers are used for producing ultrashort bunches of electrons at a repetition rate between KHz and MHz. The properties of the beam in terms of coherence and space-charge-induced energy and temporal spread are carefully controlled in order to achieve the maximum spatial and temporal resolution [11]. Fs pulses containing as few as one electron each have been used in order to minimize the mutual repulsions and obtain a coherent beam capable of a temporal resolution limited by the laser pulse duration and atomic spatial resolution [12–14]. At the same time, ultrafast processes in samples, such as phase transitions [15], melting [16] or crystallization of solids [17] and phase separation [18], and other phenomena [19], have been induced with fs laser pulses of appropriate wavelengths and intensity synchronized with the probing electron bunches through optical or electronic set-ups [17].

[a] e-mail: fabrizio.carbone@epfl.ch

Article published by EDP Sciences

1.3 TEM-based time-resolved techniques

Once the basic concepts for ultrafast electron microscopy have been established, several evolutions of the technique have been demonstrated [19]. The structural dynamics and the morphology changes of thin films have been observed in imaging with fs resolution [20,21]. In fs electron tomography, resolution in four dimensions was obtained combining fs time-resolution with 3D spatial information retrieved from a complete tilt series of 2D projections of a nanocrystal [22]. Scanning Ultrafast Electron Microscopy (SUEM) have been used for imaging nanostructures and biological specimens [23], while convergent beam electron microscopy has been used for nano-scale diffraction studies [24].

1.4 Electron energy loss spectroscopy

In a 200 keV TEM, EELS spectra can cover the range from few to thousands of eV. In the range between 1 and 50 eV, electrons loose kinetic energy exciting across-gap electron-hole pairs, excitons, defects states, atomic states and collective modes of delocalized orbital charges termed plasmons, among others. The binding energy and dispersion of the plasmon features are related to a material's lattice and its valence and conduction band electronic structure; their dynamical evolution is a manifestation of the interplay between the ions and the bonding charges [25]. In molecular systems, charge transfer losses are found in this energy window, and their dynamics is of crucial importance during chemical reactions and phase transitions [26]. At higher energies, losses from inelastic scattering from core levels are found. The binding energy of core levels is a finger-print of the different elements contained in a specimen and can be used for elemental analysis and in energy filtered imaging for element mapping [12]. Their spectral shape instead contains information about orbital occupation and spin configuration [5], in the so-called near-edge region, and about interatomic distances in the extended region [27]. Spectroscopy alone is a very powerful tool that can yield information on both the lattice and the electronic structure. Techniques delivering similar information like Non-Resonant X-ray Inelastic Scattering (NIXS), the photon equivalent of EELS, and X-ray Absortpion Spectroscopy, are also very popular and several beam-lines at synchrotrons were recently built [28]. The dynamical evolution of such a broad spectrum can reveal the changes of all these structural and electronic properties during chemical reactions and phase transitions, making time-resolved EELS a particularly appealing evolution of modern microscopy.

1.5 Time-resolved electron energy loss spectroscopy

FEELS was first demonstrated in references [29] and [30], where the evolution of the bulk plasmon of a thin film of graphite was investigated. In this contribution, a 50 eV wide spectrum was monitored with a few hundreds fs time-resolution, revealing relative shifts in the binding energies of few tens of meV and changes in the amplitude of the energy loss of few percent. Such high sensitivity corresponds to variations in the material structure of few fractions of pm and re-distributions of the orbital charge density in the order of 10^{-4} Å^{-3}. These studies demonstrated the ability of FEELS to directly capture the subtle interplay between the lattice and the electronic structure of a solid for the first time. Later, FEELS has been extended into Photon-Induced Near-field Electron Microscopy (PINEM) by imaging the electric field induced in carbon and silver nanotubes by laser light [31]; the same technique was successfully applied also to biological samples [32]. These results and their implications will be the focus of this review.

1.6 Organization of the paper

The paper will be organized as follows: in Section 2 we will describe the experimental apparatus and its performances; in Section 3 we will discuss the first FEELS experiments on graphite. In Section 4 we will review the PINEM experiments on nanotubes and biological samples, while in Section 5 we will discuss the perspectives of these studies and draw conclusions.

2 Experimental set-up

The Caltech set-up can be described as follows: a fs laser emitting 10 μJ per pulse at 1030 nm with variable pulse width (200 fs to 10 ps) and repetition rate (200 kHz to 25 MHz) was used to generate both the pump photons and the probing electrons via photoemission from a LaB_6 tip embedded in a FEG module as described in [12]; LaB_6 substitutes the usual tungsten/ZR/O tip and is a thermal emitter instead of a field emitter. The EEL spectra of the electrons transmitted through a specimen are recorded at different time delays between the pump photons and the probe, which can range from few fs to ns. Each electron bunch contains statistically one electron, corresponding to an average current of 0.16 pC at 1 MHz repetition rate, as was done also in recent imaging experiments where the UV intensity on the photocathode was lowered until no signatures of space charge effects were detectable in the TEM [20]. In this way, the broadening of the elastically transmitted electron beam, due to space-charge, is absent. This is important for obtaining the maximum energy resolution of the spectrometer. Also, space-charge effects dominate the temporal evolution of the pulses decreasing the overall time-resolution. In Figure 1, we show a schematic of the ultrafast microscope, in the inset a schematic of the electron energy loss filter is shown. A train of 220 fs laser pulses at an energy of 1.2 eV was split in two paths: one was doubled in energy for obtaining the pump pulses, while the other was tripled for photoemitting electron bunches from the photocathode. The photoelectrons were accelerated up to 200 keV. The fluence of the sample excitation ranged between tens of μJ/cm^2

https://doi.org/10.1051/epjap/2010100354 Published online by Cambridge University Press

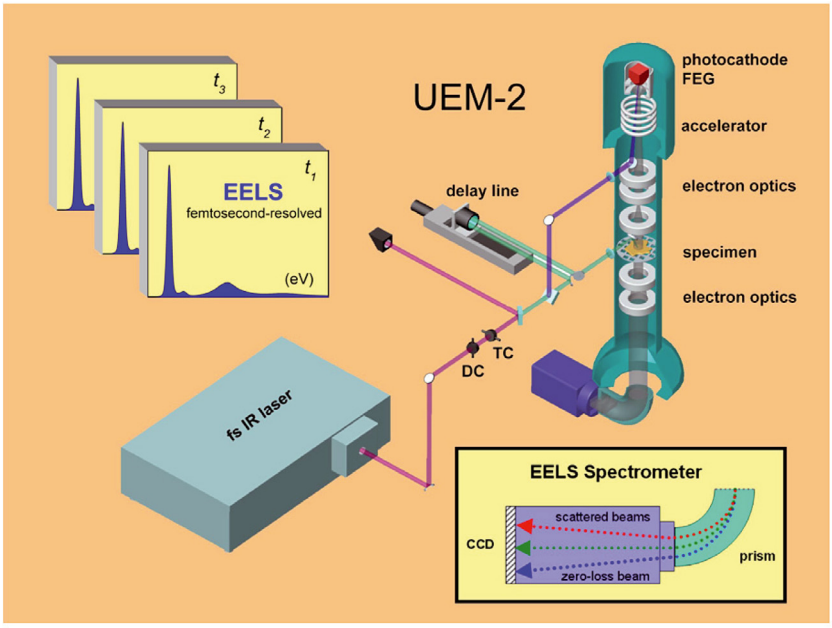

Fig. 1. (Color online) Experimental set-up. Schematic of the Caltech time-resolved TEM with a detail of the electron energy loss spectrometer. DC and TC are the doubling and tripling crystals for second and third harmonic generation. Adapted from [29].

and 5 mJ/cm^2, obtained by focussing optical pulses of different energy into a 30 μm diameter spot. Electrons were transmitted through the sample and collected by a set of magnetic lenses before being detected in a high-sensitivity CCD camera. In the microscope, one can obtain either a high resolution image of the sample, a diffraction image, or the electron energy loss spectrum. For the latter, a Gatan imaging filter (GIF) Tridiem, of the postcolumn type, was used. The zero-loss electron peak had an energy width of nearly 1 eV, comparable to that obtained in thermal-mode operation of the TEM; this value was found to increase significantly when more electrons were contained in each bunch, space-charge limited regime. The repetition rate used in most of the experiments ranged between 100 kHz and 5 MHz. This apparatus delivers approximately 250 fs time-resolution, and 1–1.5 eV total energy resolution. The spectrum at each time delay is typically recorded in a minute time of integration, and an overall temporal scan, performed stroboscopically can take few hours depending on the specimen and experimental conditions.

3 Ultrafast EELS on graphitic systems

Graphite is composed of stacked sheets of π-bonded carbon ions in a honeycomb network, termed graphene. The TEM image of a single one-atom-thick graphene sheet, taken from reference [3], is displayed in Figure 2a. Within the graphene sheets, the bonding is very strong; in fact, graphene is the toughest material known. In the perpendicular direction instead, a weak van der Waals bond holds the layers together. This strong structural anisotropy causes the transport and optical properties of the material to be rather 2-dimensional [33], and is also responsible for the coherent structural dynamics that can be induced by infrared laser pulses [34–36]. Such a two-dimensionality is responsible for the unique electronic properties of graphite and its related compounds, carbon nanotubes, fullerenes, graphene [37], as well as for its peculiar structural dynamics [29,35,36,38–42]. Graphite crystals and thin films provided the ideal material for several time-resolved microscopy experiments. The reason is that it is a very easy sample to handle, it can be prepared in flat surfaces for measurements in reflection geometry or it can be cleaved repeatedly and thinned all the way down to the single atom thickness [37]. Its surface is stable in air, and being composed solely of carbon, a relatively light element, it can be penetrated by high energy electrons for several unit cells (the typical electrons elastic mean free path is between 50 and 100 Å). Graphite is also capable of withstanding very high radiation intensity, owing to its very high melting temperature of few thousand degrees, and is in fact used in extreme conditions such as the beam dumper of the new LHC [43]. When irradiated by fs infrared pulses, damage can occur above the fluence of 170 mJ/cm^2 [40]. Its physical properties have been exploited over the years in different technological environments; graphite has been used as a dry lubricant, its fibers are commonly used for ultralight and strong components, as a shield in high radiation environment [44], and recently, applications in microelectronics and optoelectronics are being developed thanks to the spectacular electronic carrier mobility displayed under low dimensionality conditions [37,45]. For all these reasons, graphite is an ideal system to test novel experimental tools. Samples of different thicknesses and geometries can be made, ranging from an almost mono-dimensional nanotube, to a two-dimensional graphene sheet, or a 3-D bulk single

https://doi.org/10.1051/epjap/2010100354 Published online by Cambridge University Press

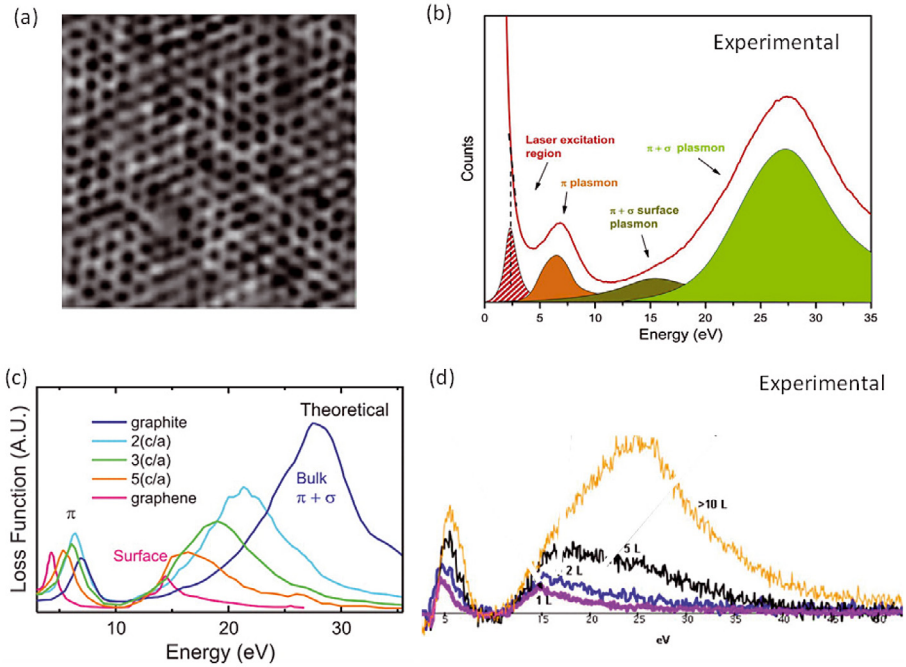

Fig. 2. (Color online) (a) TEM image of a single graphene layer, taken from [3]. (b) Experimental static plasmon spectrum of graphite, taken from [29]. (c) Theoretical plasmon spectra of graphite at different thicknesses, taken from [49]. (d) Experimental plasmon spectra in graphite at different thicknesses, data taken from [3].

crystal; being made of a light element, carbon, it is also a good test system for biological aggregates. It can be studied under very diverse irradiation conditions, and it reacts to impulsive excitation both with ultrafast electronic [46] and structural phenomena [38] and with long-term coherent vibrations [21].

3.1 The static EEL spectrum of graphite

The signatures of the above-mentioned anisotropic chemical bonds can be found in the static EELS spectrum, which is displayed in Figure 2b: the collective oscillation of the charges in the in-plane π orbitals, termed π plasmon, is found near 7 eV. At at higher energy, the peak at 27 eV is due to the bulk plasmon, and contains combined information about the charges in the σ and the π orbitals. A shoulder on the low energy side of the bulk plasmon is observed and attributed to the surface plasmon of the material. The evolution of the plasmons at different lattice parameters is displayed in Figure 2c, where we show the changes of the bulk and π plasmons when the c-axis lattice parameter is modified. When the interlayer distance is enhanced (larger c-axis), the bulk plasmon decreases, because of the decreased three-dimensionality of the solid. This behavior was experimentally confirmed by measuring few layer graphite ranging from the pure single layer graphene up to a 10 layers film. The results are displayed in Figure 2d [3]. Consistently with the theoretical calculations, in single layer graphene only the surface plasmon is observed, while the bulk plasmon gains strength in thicker films. The two-dimensionality of the material is also reflected in the experimentally measured dispersion of the π plasmon, theoretically modeled within a pure two-dimensional calculation [47]. An exhaustive discussion of the plasmons dispersion and its relation with the material dimensionality can be found in [48].

3.2 The dynamical EELS spectrum of graphite

When irradiated by ultrashort pulses of infrared light, graphite undergoes a series of peculiar structural motions. In various reports by Ultrafast Electron Crystallography (UEC) it has been shown that immediately after laser excitation the interlayer distance of the material decreases, contrary to the behavior of any known material which normally undergoes a thermal expansion when subjected to a temperature jump [38]. These results are summarized in Figure 3, where we display the c-axis lattice parameter as a function of time for an excitation fluence of 5 mJ/cm^2. The reason for this behavior is that the initial infrared excitation induces strong coherent vibrations of the ions within the graphene layers. This behavior has been reported also by means of pump-probe optical spectroscopy, photoemission, Raman and THz spectroscopy and was understood theoretically in reference [34]. Such coherent phonon behavior is evidenced in the inset of Figure 3, where the transient anisotropic reflectivity data from reference [35] are plotted together with the c-axis dynamics obtained by UEC. In these data, an ultrafast oscillation, 26 fs period, is superimposed to a slower one, 700 fs period. The fastest oscillation of the transient reflectivity is due to an in-plane coherent phonon, while the slow one is caused by

https://doi.org/10.1051/epjap/2010100354 Published online by Cambridge University Press

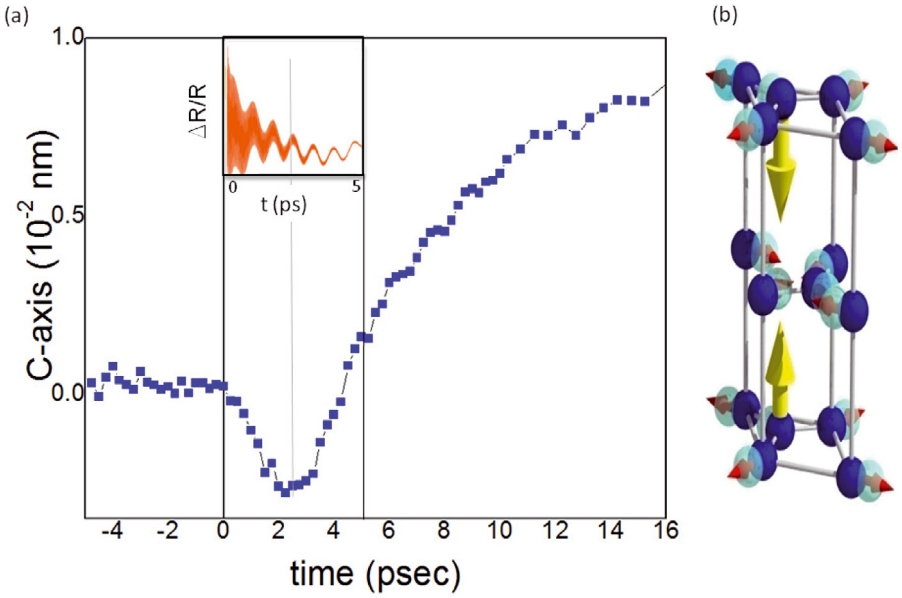

Fig. 3. (Color online) (a) Graphite *c*-axis dynamics observed by UEC [38]. In the inset we show the coherence period of the in-plane coherent phonons as measured by transient anisotropic reflectivity [35]. (b) Pictorial representation of graphite structural dynamics: the light blue spheres and the red arrows indicate the ionic motions induced by the coherent in-plane optical phonons, while the yellow vertical arrow indicates the resulting *c*-axis compression.

the out-of-plane shearing motion of the graphene sheets. It is important to notice here that the *c*-axis compression has a characteristic time comparable to the coherence time of the fast in-plane oscillation. This, in fact, is considerably dumped after about 3 ps, when the *c*-axis compression is maximum. During the coherence time of the in-plane optical phonon, carbon ions of different layers vibrate around their equilibrium positions out of phase, because it is an optical phonon, and therefore a more compact stacking is allowed in the *c*-axis direction. This is pictorially represented in the right panel of Figure 3 where the equilibrium positions of ions in the unit cell of graphite are drawn as blue spheres, while the distortion induced by the in-plane optical phonon is indicated by red arrows and light blue spheres.

The strong *c*-axis dynamics reported in diffraction, modulates the electronic structure of the material and gives a discernable signal in fs EELS. As we discussed above, the center of mass and the strength of the plasmon features depends on the structural parameters [49]. In references [29] and [30], the evolution of the EELS spectrum of graphite upon laser excitation was reported. Time-resolved EELS experiments were carried out on nm-thick single crystal of natural hexagonal graphite. The sample was cleaved repeatedly until a transparent film was obtained, and then deposited on a TEM grid; the thickness was determined from EELS to be 108 nm. The FEELS data were recorded in the UEM, operating in the single-electron per pulse mode to eliminate Boersch space charge effect. The overall energy-time changes in the FEEL spectra are displayed in Figures 4a and 4c. To make the changes more apparent, the difference between the spectra after the arrival of the initiating laser pulse (time zero) and a reference spectrum taken at 20 ps before time zero is shown. The most pronounced changes are observed in the region near the energy of the laser itself (2.39 eV), representing the energy-loss enhancement due to the creation of carriers by the laser excitation, and in the region dominated by the surface and bulk plasmons (between 13 and 35 eV). Clearly evident in the 3D plot are the energy dependence as a function of time, and the increase and decrease of the EELS signal strength [30]. In [50], these results were simulated ab-initio within the LDA-LMTO approximation. The EELS spectra were re-calculated at each value of the *c*-axis lattice parameter obtained from diffraction experiments, and the temporal evolution of the EELS signal induced by such structural distortions was simulated. The structural dynamics (compression/expansion) observed by UEC [38,51] modulates the collective excitation of the orbital charge, and induces changes in the EELS response. In particular, the bulk plasmon (feature at 27 eV) gains strength and blue-shifts during the compression; instead, during expansion, its strength decreases [49]. The region between 12 and 20 eV, most sensitive to the surface plasmon, gains spectral weight. The theoretical results are displayed in Figures 4b and 4d. The LDA-LMTO simulations satisfactorily reproduce the experimental data: (i) during compression, a large increase of the bulk plasmon strength is observed; (ii) during expansion, an increased spectral weight between 12 and 20 eV, and a decreased loss at 27 eV are found. A qualitative agreement is achieved for the π-plasmon dynamics (see the behavior of the low-energy region in the colormaps in Figures 4a and 4b). Here, we point out the sensitivity of these experiments giving some quantitative estimates of the changes observed: a *c*-axis change of 0.015 (comparable

https://doi.org/10.1051/epjap/2010100354 Published online by Cambridge University Press

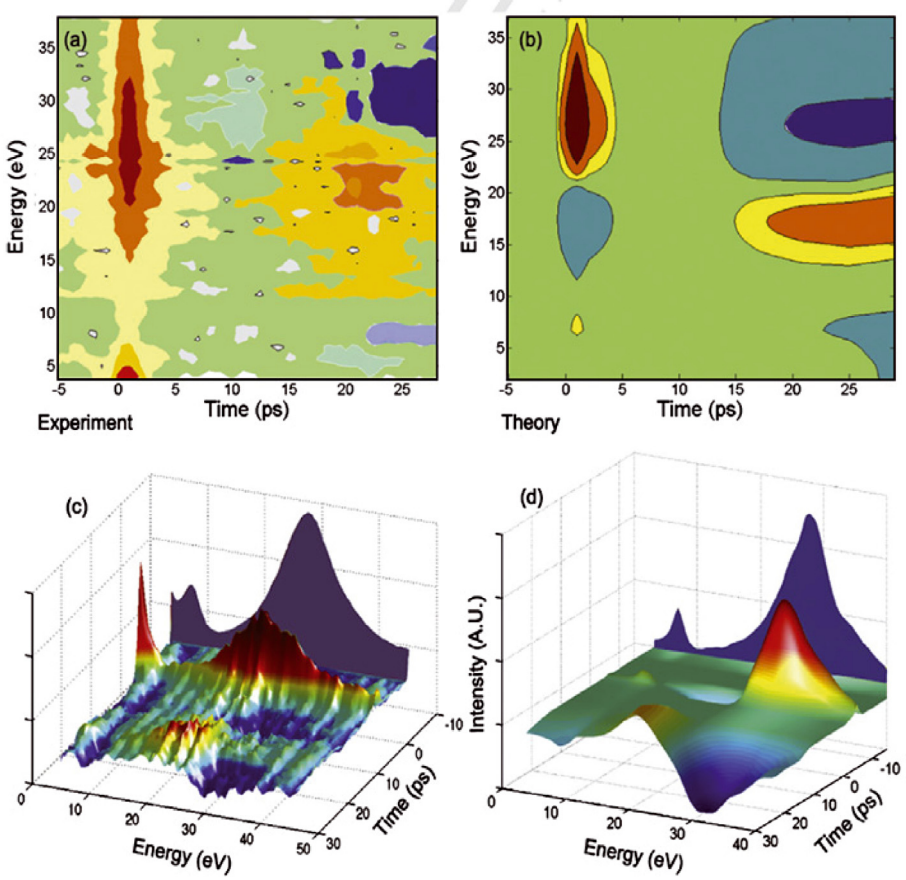

Fig. 4. (Color online) (a) Colormap of the experimental dynamical EELS obtained as EELS(t)-EELS($t < 0$). (b) Colormap of the theoretical dynamical EELS obtained as EELS (compressed/expanded) – EELS (static). (c) 3D map of the experimental dynamical EELS adapted from references [29,30]. (d) 3D map of the theoretical plasmon dynamics. These graphs are taken from [50].

to the dynamics observed in UEC [38]) induces a change of 0.5×10^{-3} Å^{-3} in the charge density [50], and consequently a change of the bulk plasmon strength around 2% and a shift of its center of mass a bit smaller then 20 meV, in agreement with what was reported in [30]. While the overall spectral resolution in FEELS experiments is in the order of 1 eV, much smaller relative shifts of the spectroscopic features can be observed by subtracting the spectra obtained at different time delays from a reference unperturbed spectrum. These results elucidated the interplay between the electronic structure and the lattice in graphite, showing the precise nature of the light-induced distortions, the direction and amplitude of atomic motion, and the consequent changes in the charge distribution.

3.3 Effect of Transient Electric Fields (TEF)

In time-resolved electron microscopy and diffraction, the use of charged particles as a probe, electrons, imposes some precautions as surface charges may deflect the probe beam giving rise to spurious effects. The use of high intensity laser pulses for photo-excitation can result in the photoemission of electrons from surfaces even when the photon energy is below the material's work function, multi-photon photoemission [52]. This is a nonlinear process where two or more photons concur in promoting a bonded electrons to the vacuum. The cross-section for such processes is usually rather small and so is the emitted charge. This emitted charge can be modeled as a small volume shaped as a disk containing a given charge propagating away from the sample surface, and its influence on the probe beam can be estimated. In a recent contribution, the impact of this effect on both ultrafast electron diffraction experiments in reflection geometry and ultrafast microscopy in transmission geometry has been evaluated [53]. In Figure 5a, we show the experimental geometry for both UEC and UEM experiments. The photoemitted charge is as a pink disk in Figure 5a, while the resulting TEF is depicted in Figure 5b. In both geometries, UEC and UEM, probe electrons pass through this area interacting with the TEF; the consequent deflections can be simulated and quantified. From these simulations it appears that this effect is irrelevant for experiments in transmission geometry while it can give a small contribution to the beam deflections observed in reflection geometry at high excitation fluence [53]. In reflection geometry, the deflection of the probe beam induced by transient

https://doi.org/10.1051/epjap/2010100354 Published online by Cambridge University Press

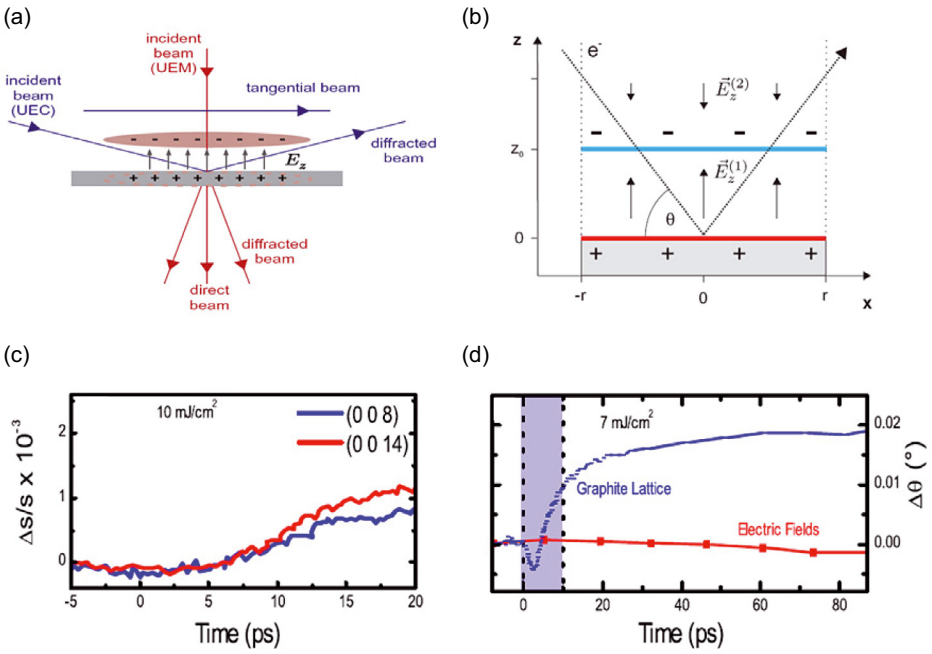

Fig. 5. (Color online) (a) Geometrical arrangement of UEC and UEM experiments and transient electric fields, adapted from [53]. (b) Schematics of the photoinduced TEF, [53]. (c) Normalized changes in the scattering vector $\Delta s/s$ for the Bragg spots (0 0 8) and (0 0 14). The changes of the diffracted beams depend linearly on the diffraction order, whereas the rise times are independent of s, as expected for structural dynamics (adapted from [53]).

electric fields on a sample surface can be investigated experimentally [54], and compared to the deflections of the Bragg diffraction spots. Such a comparison was made on a graphite surface. In Figure 5d we show the deflection of the probe-electron beam caused by TEF together with the laser-induced deflections of the Bragg diffraction peaks. One can see that the TEF induced deflection is much smaller and much slower than the dynamics of the structural changes, which also obey Bragg diffraction laws (Fig. 5c). Certainly, when using electrons as a probe, in particular in reflection geometry where electrons travel a significant amount of time close to the sample surface, extra care must be taken in estimating the effect of any possible surface charging. However, for excitation fluences below few tens of mJ/cm^2, we have experimental evidence that this effect gives only a minor contribution to the overall observed pattern modifications.

3.4 Discussion of graphite dynamics

The ultrafast dynamics of graphite has been investigated first by fs optical spectroscopy, revealing its strong coherent phonon behavior [35,36]. The mechanism for excitation of coherent phonons in graphite has been elucidated by recent time-resolved photoemission [55], THz [39], and Raman experiments as well as by new theoretical considerations [34,56]. However, the interplay between these motions and the charge carriers in the solid remained elusive. In particular, the microscopic origin of the recombination of the excited electron-hole is still debated [46,50]. Ultrafast electron diffraction evidenced for the first time that during the coherent phonons oscillation time the interlayer distance undergoes compression followed by a strong non-thermal expansion [38]. This observation is consistent with a recently proposed model for the ablation mechanism of graphene flakes from an IR irradiated graphite surface [40]; in this model, infrared laser pulses induce a strong modulation of the c-axis lattice parameter in graphite, during which the interlayer distance can be reduced to the point that graphene layers collide with each other; a strong rebound results from these collisions and causes the ablation of entire graphene sheets [40]. This peculiar ablation phenomenon was observed in separate independent experiments [41,42], where an alternative explanation based on Coulomb explosion was also proposed [41]. Moreover, it was also proposed that the strong ultarfast compression of the interlayer distance can induce the phase transformation from graphite to diamond [30,51]. The formation of diamond nanocrystals on a light irradiated surface of graphite was recently observed by means of STM [57]. In the longer time-scale, the sequence of compression/expansion of the lattice launch a sound wave in graphite membranes whose mechanical properties were investigated directly by ultrafast imaging in the UEM set-up [20,21]. In these experiments, fs

https://doi.org/10.1051/epjap/2010100354 Published online by Cambridge University Press

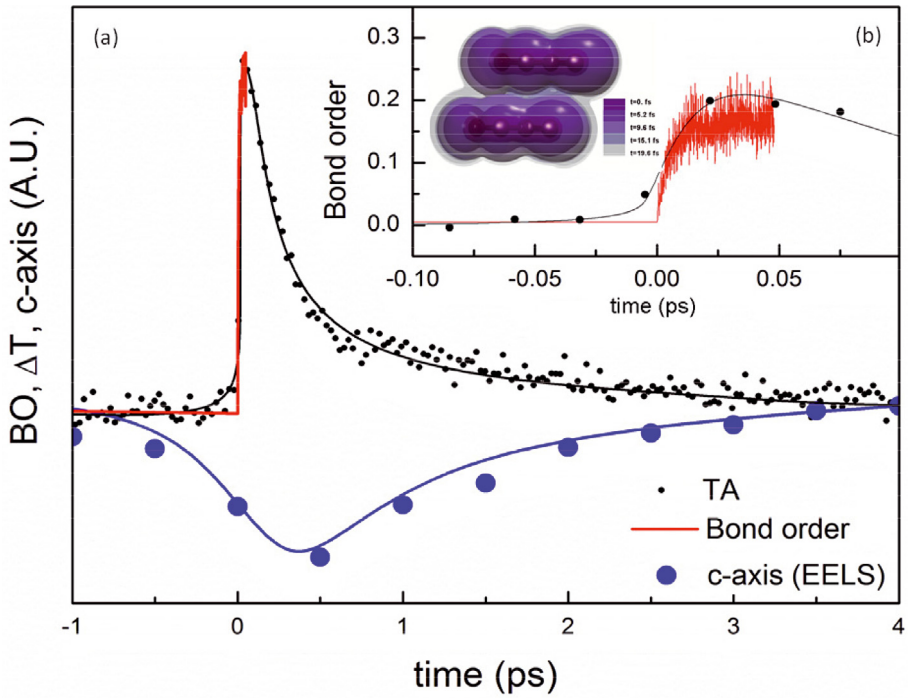

Fig. 6. (Color online) (a) Structural and electronic dynamics of graphite. The dynamics of the *c*-axis lattice parameter derived from EELS and UEC experiments is shown together with the transient optical absorption and ab-initio calculations of the photo-induced changes of the charge density in the material. In the inset (b), a detail of the ultrafast (30 fs) time-scale is shown. The ab-initio calculation is superimposed to the TA data and the evolution of the charge density is also displayed. This figure is taken from [58].

resolution in time combined to nm resolution in space was achieved, delivering important quantities like the Young modulus of the membrane and the Q-factor of the nano-mechanical resonator [21]. When combined together, the ultrafast electron diffraction, imaging and spectroscopy experiments of graphite provide a remarkably complete picture of its dynamic, both structural and electronic. In Figure 6, we summarize these findings showing in the same plot the structural response obtained from EELS and diffraction, blue symbols, and that of the electronic structure obtained by transient absorption. In the same plot, the red line is an ab-initio calculation of the change in the bond-order of graphite during laser excitation [58]. In these calculations, the change in hybridization from sp^2 to sp^3 of graphite upon laser excitation was observed and its time-scale estimated. As one can see, this time-scale is in very good agreement with the one estimated from high resolution transient absorption experiments, and coincides with the time necessary to the excited electrons to reach an equilibrium distribution. This new electronic configuration is precursor of the following coherent phonon excitation and consequent structural compression observed by EELS and diffraction.

4 Photon Induced Near-field Electron Microscopy PINEM

The possibility to combine energy filtering with imaging in modern TEM has been largely exploited by a variety of techniques for element mapping in specimens [12], plasmon imaging in nanostructures [59–61], and contrast enhanced imaging [62]. In two recent pioneering articles, the possibility to image the evolution of light-induced evanescent fields in nanostructures and biological specimens was demonstrated [31,32]. The technique, termed Photon Induced Near-field Electron Microscopy (PINEM), takes advantage of the interaction between the laser field and electrons mediated by a specimen. In the ultrafast transmission electron microscope, as described above, electron and photon pulses can be overlapped spatially and temporally. While in vacuum no interaction is possible between them due to energy-momentum conservation rules, interaction with a medium can promote exchange of energy between photons and electrons. The detected electron beam in UEM can be energy filtered, revealing the energetics of such an interaction, and thanks to sophisticated collecting optics, even it spatial properties.

4.1 PINEM on carbon and silver nanotubes

The PINEM effect was first reported in carbon and silver nanotubes [31], where fs light pulses induced an evanescent field in the nanotube which was directly imaged by probe electron pulses. In Figure 7a, a conceptual drawing of the experiment is shown. When light excites the nanotubes earlier than the arrival of the electron pulse, at $t < 0$, obviously no interaction takes place. At coincidence, $t \geq 0$, the electrons interact with the evanescent field induced by photons and can either gain or loose quanta

https://doi.org/10.1051/epjap/2010100354 Published online by Cambridge University Press

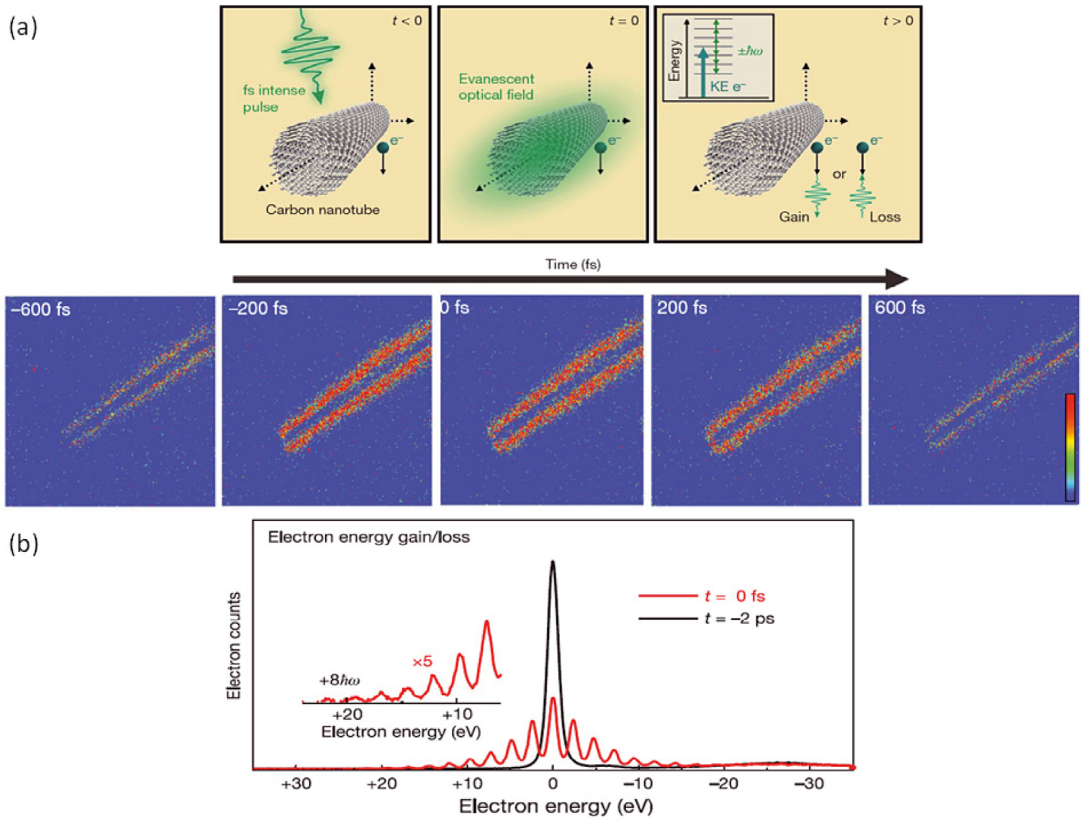

Fig. 7. (Color online) (a) Top panel: the interaction between light and electrons in a carbon nanotube is shown in a schematic of the PINEM experiments. Bottom panel: temporal evolution of the photo-induced near field around the nanotube. (b) The spectra of the probe electrons are shown before and right after the arrival of the pump photons. These graphs are adapted from [31].

of energy corresponding to that of the exciting photons. The spectrum of the probe electrons after the interaction with light in the nanotube is shown in Figure 7b. The elastic peak, containing information about electrons scattered without loss of energy, is strongly depleted and several satellites are observed at energies corresponding to the absorption of multiple integers of the single light quantum $\hbar\omega = 2.3$ eV. At higher energies, the typical features of the material, plasmons and interband transitions are observed. The electrons that have gained energy interacting with the photo-induced field can be selected by filtering and used to form images of the evanescent field around the nanotube. In fact, only the electrons traveling close to the nanostructure surface can gain energy. Such images are shown in the lower panel of Figure 7a at different time-delays between the pump photons and the probe electrons. These images provide a direct observation of photo-induced fields in a nanostructure, in this case a carbon or a silver nanotube (see online support material of [31]). The dependence of the photo-induced near field on the light polarization direction with respect to the nanotube was also shown, reveling the effect of confinement. In fact, when the electric field of the photons was polarized perpendicular to the length of the nanotube, an enhancement of the induced field was observed and attributed to the particular spatial distribution of the field modes in the regime where the material dimension d is smaller than the wavelength λ [31]. In general, the precise field distribution depends on the geometry of the nano-structure, and therefore the polarization dependence could be exploited ad hoc in complex systems to evidence sub-structures.

4.2 PINEM on biological samples

The PINEM technique can also be successfully applied for imaging biological samples. In particular, the interaction between photons and electrons mediated by a nano-sized object, such as protein vesicles or an *Escherichia coli* in [32], can be used in order to enhance the contrast in imaging surfaces [32]. The strength of the PINEM signal depends on the number of photons interacting with the electron packets, even if not directly absorbed by the specimen. Therefore, even at high photons flux, a medium that is transparent at a given photon energy can be imaged by PINEM without photo-induced damage. This, combined with the low energy deposited by electrons per inelastic scattering events in materials [28], and the low current inherent to ultrafast electron microscopy, makes this technique particularly suitable for the study of biological samples. Most importantly, these contrast-enhanced images can be obtained with fs temporal resolution,

https://doi.org/10.1051/epjap/2010100354 Published online by Cambridge University Press

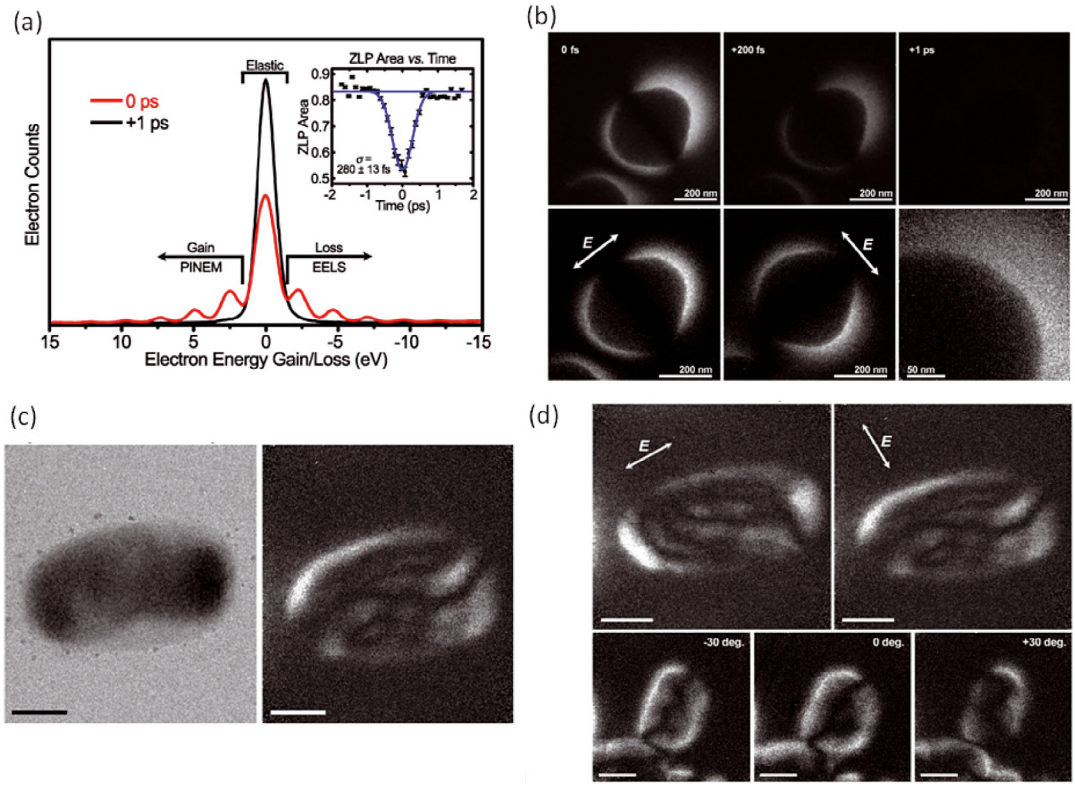

Fig. 8. (Color online) (a) PINEM effect on protein vesicles. (b) temporal (top) and polarization (bottom) evolution of the PINEM effect in protein vesicles. (c) Comparison between a bright field image of *E. Coli* (left) and the PINEM image (right). (d) Polarization dependence of the PINEM images (top), and tomographic images at different tilt angles (bottom). These graphs are adapted from [32].

reveling details of the dynamics of the fields on the imaged surfaces. Surface fields and their dynamics, in turn, depend also on the dielectric or conducting properties of the surfaces. In Figure 8, the results of the experiments on biological samples are summarized. In Figure 8a, the PINEM effect on protein vesicles is reported. As for nanotubes, the elastic peak is split into several satellites spaced by the energy of the photons. Images were taken by filtering all electrons that have gained energy in the interaction with photons in order to enhance contrast at the surface of the specimen. In Figure 8b we show the temporal and polarization dependence of the PINEM images from the protein vesicles. It is worth noticing here that contrast is enhanced in imaging principally at the outer shell of the vesicle. This is due to the thickness and dielectric properties of the protein membrane that does not allow the electric field to penetrate. In Figure 8c instead, we show the comparison between a standard bright-field image of an *E. Coli* and the PINEM image. With respect to PINEM experiments on protein vesicles, contrast enhancement is obtained both at the surface and inside the cell, because of the thinner structures of the *E. Coli* [32]. Also, in Figure 8d, a tomographic analysis of the cell was performed by recording PINEM images at different angles of incidence of the probe electron beam, demonstrating the ability of the technique to deliver volumetric information about the cell surface structure.

5 Perspectives and conclusions

Time-resolved electron microscopy has demonstrated a unique versatility, allowing breakthrough discoveries in solids [15,30], nanostructures [31], membranes [21], and biological aggregates [32]. After the successful results obtained on relatively simple systems, such as graphite for example, which allowed to calibrate and consolidate the experimental tools, more complex analysis and problems can be attacked. From the technical point of view, improvements of the main properties, time-resolution, spatial coherence and contrast to magnetic structures, and acquisition time, of electron-based instruments are already on the way. Recent studies addressed the possibility to push temporal resolution even in the attosecond domain [63]. Also, new sources for enhanced coherence have been proposed based on the use of Bose-Eisntein condensates [64,65], and single shot electron diffraction with 200 fs electron bunches has been demonstrated via the use of relativistic electrons [66], and by radiofrequency compression of 100 kV electron [67]. The perspective for these tools is vast, and applications range from condensed matter long-standing problems like high temperature superconductivity [68,69], to the study of magnetic phenomena like superconducting vortexes or domains in nanostructures by Lorentz microscopy [70,71], and to the unraveling of biological functions in cells [32].

https://doi.org/10.1051/epjap/2010100354 Published online by Cambridge University Press

FC acknowledges prof. A.H. Zewail, prof. M. Chergui for useful discussions, and G. Mancini for careful reading of the manuscript. This work was financially supported by the Swiss National Science Foundation.

References

1. E. Ruska, *The early development of electron lenses and electron microscopy* (Hirzel Verlag, Stuttgart, 1980)
2. A.V. Crewe, M. Isaacson, D. Johnson, Rev. Sci. Instrum. **40**, 241 (1969)
3. T. Eberlein et al., Phys. Rev. B **77**, 233406 (2008)
4. D.L. Dorset, W.F. Tivol, J.N. Turner, Ultramicroscopy **38**, 41 (1991)
5. C. Jeanguillaume, P. Trebbia, C. Colliex, Ultramicroscopy **3**, 237 (1978)
6. C. Colliex, Nature **450**, 622 (2007)
7. H. Kurata, C. Colliex, Phys. Rev. B **48**, 2102 (1993)
8. P.W. Hawkes, J.C.H. Spence, *Science of Microscopy. Imaging and microscopy* (Springer, New York, 2007)
9. A.H. Zewail, Science **328**, 187 (2010)
10. D. Shorokhov, A.H. Zewail, Phys. Chem. Chem. Phys. **10**, 2879 (2008)
11. A. Gahlmann, S.T. Park, A.H. Zewail, Phys. Chem. Chem. Phys. **10**, 2894 (2008)
12. H.S. Park, J.S. Baskin, O.H. Kwon, A.H. Zewail, Nano Lett. **7**, 2545 (2007)
13. V.A. Lobastov, J. Weissenrieder, J. Tang, A.H. Zewail, Nano Lett. **7**, 2552 (2007)
14. O.H. Kwon, B. Barwick, H.S. Park, J.S. Baskin, A.H. Zewail, PNAS **105**, 8519 (2008)
15. M.S. Grinolds et al., PNAS **103**, 18427 (2006)
16. B.J. Siwick et al., Science **302**, 1382 (2003)
17. O.H. Kwon et al., PNAS **105**, (2008)
18. J.S. Kim et al., Science **321**, 1472 (2008)
19. A.H. Zewail, J.M. Thomas, *4D Electron Microscopy: Imaging in Space and Time* (Imperial College Press, London, 2010)
20. B. Barwick, H.S. Park, O.-H. Kwon, J.S. Baskin, A.H. Zewail, Science **322**, 1227 (2008)
21. O.H. Kwon et al., Nano Lett. **8**, 3557 (2008)
22. O.H. Kwon, A.H. Zewail, Science **328**, 1668 (2010)
23. D.-S. Yang, O.F. Mohammed, A.H. Zewail, PNAS (2010), www.pnas.org/cgi/doi/10.1073/pnas.1009321107
24. A. Yurtsever, A.H. Zewail, Science **326**, 708 (2009)
25. J. Nelayah et al., Nat. Phys. **3**, 348 (2007)
26. D. Schmeisser, J.E. Demuth, Ph. Avouris, Chem. Phys. Lett. **87**, 324 (1982)
27. T. Fujikawa, T. Miyanaga, J. Phys. Soc. Jpn **62**, 4108 (1993)
28. M. Chergui, A.H. Zewail, Chem. Phys. Chem. **10**, 28 (2010)
29. F. Carbone et al., Chem. Phys. Lett. **468**, 107 (2008)
30. F. Carbone, O.H. Kwon, A.H. Zewail, Science **325**, 181 (2009)
31. B. Barwick et al., Nature **462**, 902 (2009)
32. D. Flannigan, B. Barwick, A.H. Zewail, PNAS **107**, 9933 (2010)
33. A.B. Kuzmenko, E. van Heumen, F. Carbone, D. van der Marel, Phys. Rev. Lett. **100**, 117401 (2008)
34. R. Saito et al., Phys. Rev. Lett. **88**, 027401 (2001)
35. K. Ishioka et al., Phys. Rev. B **77**, 121402(R) (2008)
36. T. Mishina, K. Nitta, Y. Masumoto, Phys. Rev. B **62**, 2908 (2000)
37. K.S. Novoselov et al., Science **306**, 666 (2004)
38. F. Carbone, P. Baum, P. Rudolf, A.H. Zewail, Phys. Rev. Lett. **100**, 035501 (2008)
39. T. Kampfrath, L. Perfetti, F. Schapper, C. Frischkorn, M. Wolf, Phys. Rev. Lett. **95**, 187403 (2005)
40. H.O. Jeschke, M.E. Garcia, K.H. Bennemann, Phys. Rev. Lett. **87**, 015003 (2001)
41. M. Lenner, A. Kaplan, R.E. Palmer, Appl. Phys. Lett. **90**, 153119 (2007)
42. A. Kaplan, M. Lenner, R.E. Palmer, Phys. Rev. B **76**, 073401 (2007)
43. S. Peraire, J.M. Zazula, LHC-Project-Report-87, 1996
44. M.S. Dresselhaus et al., *Graphite Fibers and Filaments*, in *Springer Series in Materials Science* (Springer-Verlag, Berlin, 1988)
45. Q. Bao et al., Phys. Opt (2010), `arXiv:1007.2243`
46. M. Breusing, C. Ropers, T. Elsaesser, Phys. Rev. Lett. **102**, 086809 (2009)
47. M.F. Lin et al., Phys. Rev. B **55**, 13961 (1997)
48. A. Gruneis et al., Phys. Rev. B **78**, 205425 (2008)
49. A.G. Marinopoulos, L. Reining, A. Rubio, V. Olevano, Phys. Rev. B **69**, 245419 (2004)
50. F. Carbone, Chem. Phys. Lett. **496**, 291 (2010)
51. R.K. Raman et al., Phys. Rev. Lett. **101**, 077401 (2008)
52. F. Banfi et al., Phys. Rev. Lett. **94**, 037601 (2005)
53. S. Schäfer, W. Liang, A.H. Zewail, Chem. Phys. Lett. **493**, 11 (2010)
54. F. Carbone, P. Baum, P. Rudolf, A.H. Zewail, Phys. Rev. Lett. **105**, 059604 (2010)
55. G. Moos, C. Gahl, R. Fasel, M. Wolf, T. Hertel, Phys. Rev. Lett. **87**, 267402 (2001)
56. T.E. Stevens et al., Phys. Rev. B **65**, 144304 (2002)
57. J. Kanasaki, E. Inami, K. Tanimura, H. Ohnishi, K. Nasu, Phys. Rev. Lett. **102**, 087402 (2009)
58. A. Acocella, F. Carbone, F. Zerbetto, J. Am. Chem. Soc. **132**, 12166 (2010)
59. P.M. Ajayan et al., Science **265**, 1212 (1994)
60. D. Ugarte, C. Colliex, P. Trebbia, Phys. Rev. B **45**, 4332 (1992)
61. M. Kociak, L. Henrard, O. Stephan, K. Suenaga, C. Colliex, Phys. Rev. B **61**, 13936 (2000)
62. L. Reimer, I. Fromm, I. Naundorf, Ultramicroscopy **32**, 80 (1990)
63. P. Baum, J. Manz, A. Schild, Sci. China **53**, 987 (2010)
64. M.P. Reijnders et al., Phys. Rev. Lett. **102**, 034802 (2009)
65. S.B. van der Geer, M.J. de Loos, E.J.D. Vredenbregt, O.J. Luiten, Microsc. Microanal. **15**, 282 (2009)
66. P. Musumeci, J.T. Moody, C.M. Scoby, M.S. Gutierrez, M. Westfall, Appl. Phys. Lett. **97**, 063502 (2010)
67. T. van Oudheusden et al., J. Appl. Phys. **102**, 093501 (2007)
68. F. Carbone, D.-S. Yang, E. Giannini, A.H. Zewail, PNAS **105**, 20161 (2008)
69. N. Gedik, D.-S. Yang, G. Logvenov, I. Bozovic, A.H. Zewail, Science **316**, 425 (2007)
70. K. Harada et al., Phys. Rev. Lett. **71**, 3371 (1993)
71. H.S. Park, J.S. Baskin, A.H. Zewail, Nano Lett. **10**, 3796 (2010)